UNIVERSITY OF AMSTERDAM

UvA-DARE (Digital Academic Repository)

Organotin photoresists for extreme ultraviolet lithography

Zhang, Y.

Publication date
2019

Document Version
Other version

License
Other

Link to publication

Citation for published version (APA):
Zhang, Y. (2019). *Organotin photoresists for extreme ultraviolet lithography*. [Thesis, fully internal, Universiteit van Amsterdam].

General rights
It is not permitted to download or to forward/distribute the text or part of it without the consent of the author(s) and/or copyright holder(s), other than for strictly personal, individual use, unless the work is under an open content license (like Creative Commons).

Disclaimer/Complaints regulations
If you believe that digital publication of certain material infringes any of your rights or (privacy) interests, please let the Library know, stating your reasons. In case of a legitimate complaint, the Library will make the material inaccessible and/or remove it from the website. Please Ask the Library: https://uba.uva.nl/en/contact, or a letter to: Library of the University of Amsterdam, Secretariat, Singel 425, 1012 WP Amsterdam, The Netherlands. You will be contacted as soon as possible.

UvA-DARE is a service provided by the library of the University of Amsterdam (https://dare.uva.nl)

Download date:09 Mar 2023

Chapter 2

Experimental methods

This chapter describes the experimental methods used in the research described in this thesis. This includes preparation of photoresist thin film samples, their exposure to electron beams and to deep ultraviolet (DUV) and extreme ultraviolet (EUV) light, and characterization of the films before and after exposure. In most of the work, we focus on tin-oxo cage molecules as photoresist models, as discussed in Chapter 1. These compounds were synthesized in our laboratory by Jarich Haitjema. In Chapter 9, commercial tin(II)carboxylates are explored.

Photoresist samples are prepared as thin films on flat and smooth substrates by means of spin coating. Different substrates are used depending on the application or the analysis method to be used: quartz substrates, which are UV-transparent, are used for UV-vis absorption spectroscopy; double side polished Si wafers and CaF_2 substrates, which are IR-transparent, are used for FTIR spectroscopy; bare Si wafers or Si wafers coated with HMDS are used as substrate for patterning; Si wafers coated with Cr (2 nm) and Au (18 nm) as conductive substrate are used for X-ray photoelectron spectroscopy. The topography and the surface roughness of the sample are characterized using atomic force microscopy (AFM). After the thin film is prepared, various exposure methods are used to investigate the response of the photoresist. For 225 nm deep ultra violet (DUV) exposure a laser was used, or Laser Driven Light Source System with a monochromator. Extreme ultraviolet (EUV) radiation (13.5 nm; 92 eV) was obtained from the EUV interference lithography tool at the Swiss Light Source XIL-II beamline (Paul Scherrer institute, PSI, Villigen, Switzerland). For electron beam exposure (E-beam) an e-beam lithography tool was used. After development and other follow-up processes such as rinse, post exposure bake (PEB), and hard bake (HB), the patterns of the photoresists were characterized by using AFM and scanning electron microscopy. In order to gain information on the photochemical conversion in the photoresist, UV-vis spectroscopy, IR spectroscopy, mass spectrometry, and photoelectron spectroscopy were used to characterize the chemical properties of the photoresist both before and after EUV/DUV exposure. Combining the above characterization methods, the properties and the chemical changes of the photoresist were evaluated. In this chapter, we briefly introduce the working principles and implementations of the most important tools and techniques used in this research.

2.1 Spin coater

As it was explained in Chapter 1, photoresists materials are applied as thin films on a substrate by spin coating. Typically, the film thickness required is several tens of nanometers. Ideally, the surface roughness (R_q) of the photoresist thin film should be below 0.5 nm, due to the requirement to write high-resolution patterns on it. In order to meet this requirement, different spin coating parameters need to be optimized, such as the spin coating speed, acceleration, spinning time, solvent, and surface tension of the substrate.

Spin coating has been widely used in the semiconductor industry as a method to prepare uniform thin films on flat substrates. The photoresist material is dissolved in an organic solvent and a certain amount of the solution is applied on the substrate. The spin coater accelerates the substrate to a high rotation speed, and the majority of the solution will be flung off the substrate. At the same time, the high-speed airflow above the substrate can remove the remaining solvent from the thin film and leave the photoresist layer. Using this simple and easy method, a homogeneous, uniform thin film of photoresist can be deposited on the substrate. The spin coating process is illustrated in Scheme. 2.1.[1]

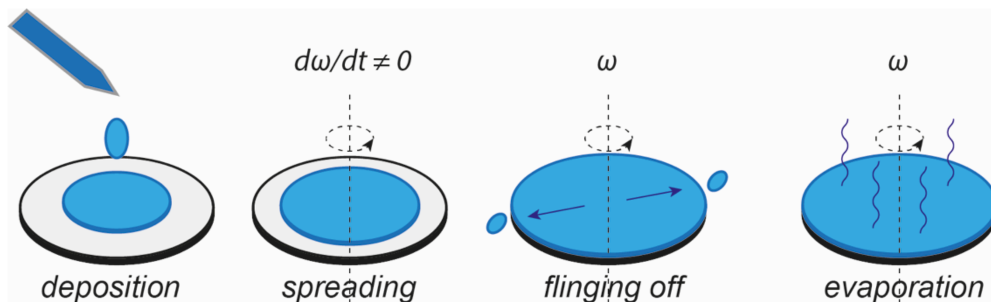

Scheme 2.1. *Spin coating process.*

The film thickness (l) is proportional to the concentration of the solution (c) and to the inverse square root of the spinning speed (angular velocity) ($1/\sqrt{\omega}$). Compared with the spinning speed, the concentration of the solution plays a more important role in determining the film thickness obtained. The spin speeds chosen determine the range of the film thickness that can be realized from a certain solution. The film thickness will also depend on the solvent viscosity, vapor pressure, local temperature and humidity. Therefore, the film thickness curve of a certain material is determined empirically. At low concentrations, the film thickness depends approximately linearly on the solution concentration. In this thesis, we prepared the tin-oxo cages into thin films for different purposes; we mainly controlled the concentration of the solution. Here, we use the tin-oxo cages with hydroxide

counterion (TinOH) as an example. The compound is a powder that was dissolved in toluene at different concentrations and spin coated with the same spin coating parameters (acceleration 700 rpm s^{-1}, final speed 2500 rpm for 35 s) on the Si substrate. The relationship between the film thickness and the solution concentration as determined using AFM (section 2.2), is shown in Fig. 2.1. Importantly, we find that the spin coating procedure is well reproducible, also on different spin coaters in different laboratories.

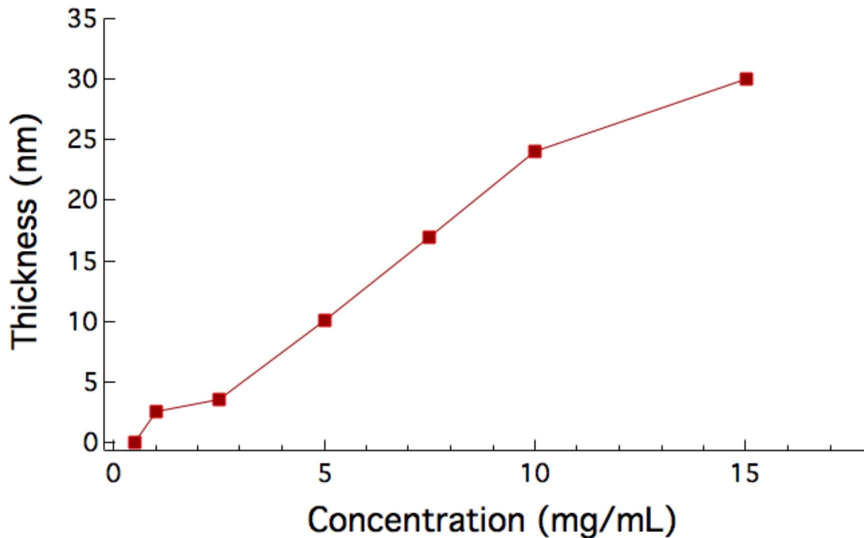

Figure 2.1. *Thickness of TinOH films vs. concentration (in toluene) for a fixed set of spin coating parameters.*

2.2 AFM

The topography and the surface roughness of the sample are usually characterized by means of atomic force microscopy (AFM). AFM is a high-resolution imaging technique with a small probe (tip) scanning back and forth in a controlled manner across a sample to measure the surface topography at up to atomic resolution. A laser beam deflection system is equipped in AFM, where a laser is reflected from the back of the reflective AFM cantilever onto a position-sensitive detector. AFM relies on the forces between the tip and the sample surface, by measuring the deflection of the cantilever. The force (F) can be calculated by using Hooke's law (eq. 2.1) where z indicates the bending, and k the stiffness of the cantilever.[2]

$$F = -kz \tag{2.1}$$

There is a feedback loop using the laser deflection to control the force and tip position. As the tip interacts with the sample surface, either controlling the force F

(corresponding to contact mode) or the position *z* (corresponding to tapping mode), the laser position on the detector can be used in the feedback loop to trace the surface topography and generate images. The working principle of AFM is shown in Scheme 2.2.

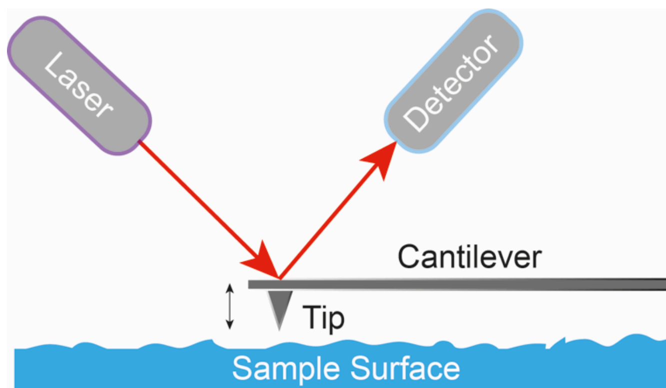

Scheme 2.2. *Schematic for Atomic Force Microscopy.*

In our experiments we used the ScanAsyst-Air mode with a silicon tip on a Nitride cantilever in Bruker Dimension Icon AFM. The ScanAsyst mode is developed based on the Peakforce tapping mechanism, which decouples cantilever response from resonance dynamics, to adjust all critical imaging parameters automatically.

The film prepared from spin coating can be characterized by AFM. To measure the film thickness, a scratch is made through the thin film, and AFM is used to scan across the edge of the scratch. The surface roughness of the thin film, which is characterized as the root-mean square roughness (R_q), also needs to be controlled in the thin film preparation procedure and can be derived from AFM measurement. The chemical compatibility of the substrate and the solution is important for the formation of a smooth spin-coated film. When the solvent and the substrate are both hydrophobic or hydrophilic, the solution will spread across the surface.[1] To illustrate this, solutions of TinOH in different solvents (isopropanol, 2-butanol and toluene) were spin-coated on silicon with a native oxide layer (hydrophilic) and on a silicon/silicon oxide substrate that was previously allowed to react with hexamethyldisilazane (HMDS) to make it hydrophobic. The surface topography of the different samples was imaged with AFM as shown in Fig. 2.2.

As is shown in Fig. 2.2, the topographies of the TinOH thin films under different preparation conditions are quite different. Comparing the three samples in a), b) and c), in polar solvent as IPA and 2-butanol, the topography of the thin film looked really rough and seems to form crystallized structures in a), and holes in b). In c) the surface also shows some larger structures, but the surface roughness and height

difference are smaller than in a) and b). Based on the condition in c), we tried to optimize the process again. Firstly, a post apply bake step (PAB) was added and afterwards the topography is shown in d). The height difference becomes smaller, but the large structure was still observed. A further optimization was done on the substrate. By modifying the substrate to make it very hydrophilic using oxygen plasma treatment or hydrophobic using HMDS, the final surface roughness of the sample was improved significantly to R_q < 0.5 nm as shown in e) and f). The possible reason could be that the tin-oxo cages contain hydrophobic components (butyl chains) and hydrophilic groups, which help it deposit on hydrophobic/hydrophilic surface homogeneously. Since the HDMS treatment is easier to apply, we used this method to prepare thin films for all further experiments, such as to test the tin-oxo cages performance under EUV/DUV/E-beam lithography.

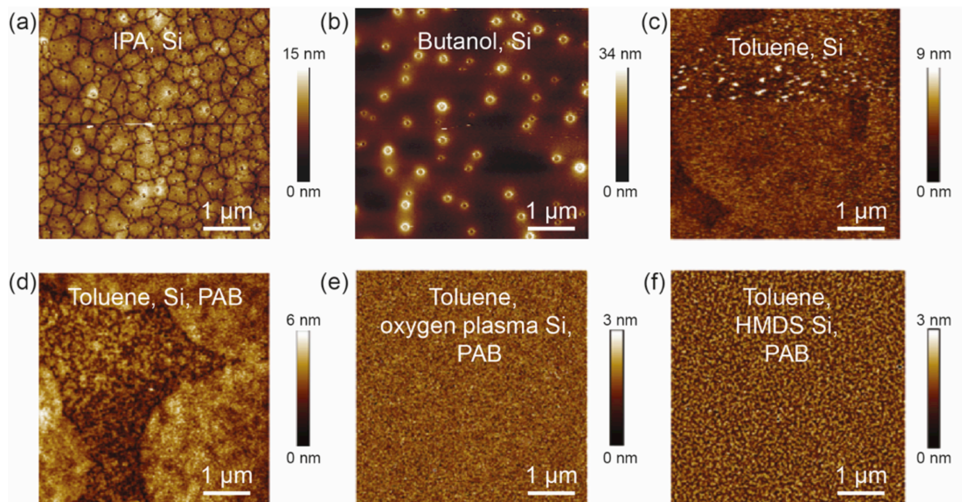

Figure 2.2. *Topography of TinOH films (a-d) on a non-treated Si substrate prepared from solutions (a) in isopropanol (IPA), (b) in butanol, (c) in toluene, (d) in toluene followed by a post application bake (PAB) step; (e) on oxygen plasma treated Si wafer in toluene and followed by a PAB step, (f) on HMDS surface treated Si wafer in toluene with PAB.*

2.3 E-beam lithography

Electron-beams are often used as a surrogate for other high-energy radiation patterning, because when using high energy photons the chemical changes are caused mostly by secondary electrons, as discussed in Chapter 1, which are also the main chemical agents arising from electron beam irradiation. In this work, E-beam lithography was performed using the Raith Voyager at the Amsterdam Nanocenter (AMOLF). The beam energy was up to 50 keV and the current range was from 50

pA to 40 nA. The beam size can be less than 2.5 nm. E-beam lithography was used to test the dual-tone pattern performance of the tin-oxo cages resist in Chapter 8.

2.4 EUV interference lithography

As mentioned above, we use extreme ultra violet interference lithography as a patterning method to test the performance of the tin-oxo cages as EUV photoresists. After preparing the photoresist amorphous thin film, the photoresist layer can be exposed to the interference pattern of coherent beams that form a parallel wave and hence an optical pattern featuring intensity peaks and valleys. In this research, we used the EUV interference lithography tool at the Swiss Light Source XIL-II beamline (Paul Scherrer institute, PSI, Villigen, Switzerland).[3-5] The working principle of EUV interference lithography is described in references [3, 4]. The incident beam from the synchrotron source passes through two diffracting gratings (Cr/Mo based) on the Si_3N_4 membrane, generating the interference pattern from the two first-order diffracted beams on the photoresist layer. The dose on the mask and the dose on the sample can be measured and controlled. The scheme of the two-beam EUV transmission-diffraction interference lithography method for patterning line-space structure is shown in Scheme 2.3.

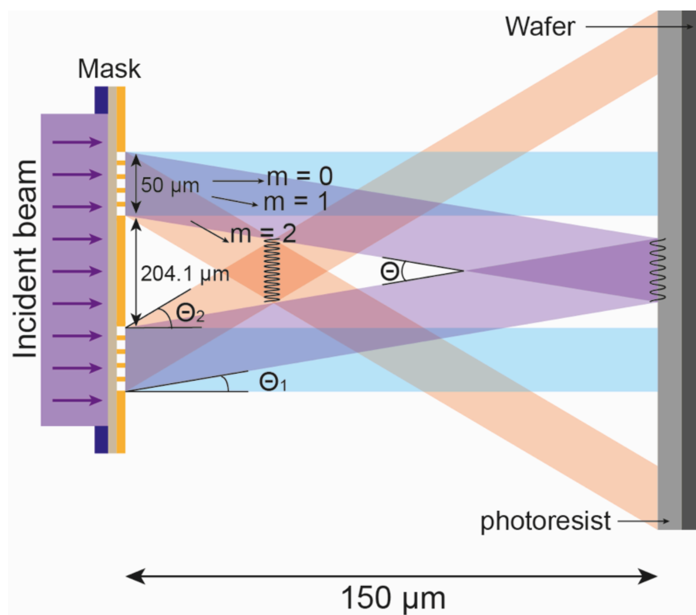

Scheme 2.3. *EUV interference lithography. Only the 1st and 2nd order diffractions interfering beams at angles Θ_1 and Θ_2 are illustrated. The diffracted beams that diverge are omitted here.[3] The physical dimension is depending on the specific mask; here we use an example from reference 6.*

As explained in reference 5, when the incident beam arrives at the mask and passes through the grating, it is diffracted by each grating in certain angles Θ_m given by:

$$sin\Theta_m = m\lambda/P_g \tag{2.2}$$

In eq. 2.2 m is the diffraction order and P_g is the grating periodicity. When the two gratings are illuminated with the same intensity, in the area where the diffracted beams interfere the periodicity (pitch) P of the aerial image is given by eq. 2.3.

$$P = \frac{\lambda}{2\sin\left(\frac{\Theta}{2}\right)} \tag{2.3}$$

Since λ = 13.5 nm, the pitch can be as small as ~7 nm, which is half of the wavelength. In equation 2.3, Θ is the angle between the two diffracted beams and in the case of two beams as in Fig. 4, $\Theta = 2\Theta_m$, and therefore, combining equations 2.2 and 2.3, we arrive at equation 2.4.

$$P = P_g/2m \tag{2.4}$$

The size and shape of the exposed pattern is the same as the size and shape of the gratings, but the line pattern of the grating is demagnified. It is common practice to describe the resolution of a lithography method by the half pitch (*HP*) of the pattern it generates. In the interference lithography with $m = 1$, the resolution of the pattern will be $HP = P_g/4$. For example: $P_g = 72$ nm gratings on mask can make a $HP = 18$ nm structure on wafer. Thus, in addition to the incident beam wavelength, which is determined by the light source, the line spacing of the grating is another essential component for high-resolution interference lithography.

The photon flux of the beam is between 20 and 50 mW cm^{-2}. By controlling the exposure time, the dose on the sample can be controlled. The exposure is done in the end station chamber with 10^{-7} mbar vacuum. High resolution patterns with 6 nm half pitch have been demonstrated in this set up.[6]

2.5 DUV exposure

A YAG-pumped OPA laser (Ekspla NT342B, University of Amsterdam), delivering nanosecond pulses at 225 nm at 10 Hz (2.5 mJ/pulse) was used as the irradiation source. The irradiated spot was approximately round, with an area of around 0.2 cm^{-2}. Alternatively, a continuous light source was used consisting of an Energetiqs EQ-99X Laser Driven Light Source System with a TRIAX190 monochromator. Using a band pass of 10 nm, this delivers 0.2 mW cm^{-2} at the sample.

2.6 Scanning Electron Microscopy

After development and other subsequent processes (such as rinse, post exposure bake, and hard bake), the patterns' quality on the different photoresists was evaluated by means of scanning electron microscopy (SEM). The SEM generates images by scanning the sample with a high-energy beam of electrons. As the electrons interact with the sample they produce secondary electrons, backscattered electrons, Auger electrons, characteristic X-rays and cathodoluminescence. Usually, the secondary electrons or the backscattered electrons are collected by detectors and the resulting signals are converted into images. The SEM schematic is shown in Scheme 2.4.

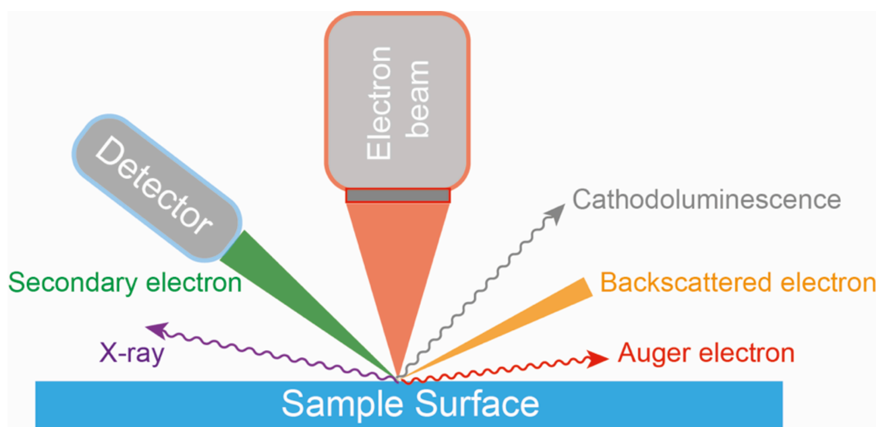

Scheme 2.4. *Schematic of a SEM.*

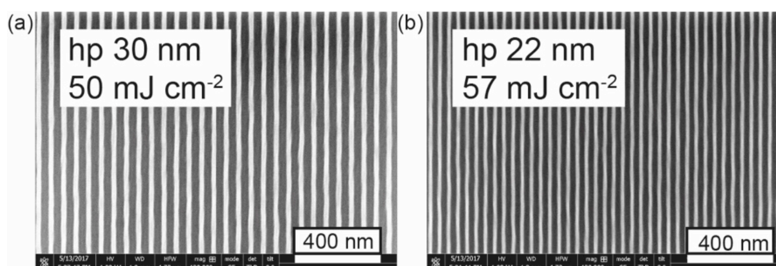

Figure 2.3. *SEM images of TinOH photoresist patterned by means of EUV interference lithography.*

In this work, SEM was performed on a FEI Verios 460 at Amsterdam nanocenter (AMOLF). In addition to AFM, which is mainly the tip diameter that limits the measurement accuracy,[7] SEM was used to characterize the line patterns of the photoresist. A significant issue of SEM is the sensitivity of photoresist to beam damage.[8, 9] To decrease the damage caused by the electrons on the photoresist

pattern while scanning, all the SEM in this thesis is taken at a relatively low acceleration potential of 1 kV and a moderate current of 50 nA. The SEM is used to characterize the pattern generated from the EUV interference lithography, and an example is shown in Fig. 2.3.

2.7 X-ray Photoelectron Spectroscopy

In order to obtain information on the chemical conversion in the photoresists thin film upon irradiation, extremely sensitive analysis techniques are required. X-ray photoelectron spectroscopy (XPS) is a widely used surface-sensitive technique and it plays a key role in the research described in this thesis.[10] It can be applied to a broad range of materials and can provide quantitative chemical state data of the samples.

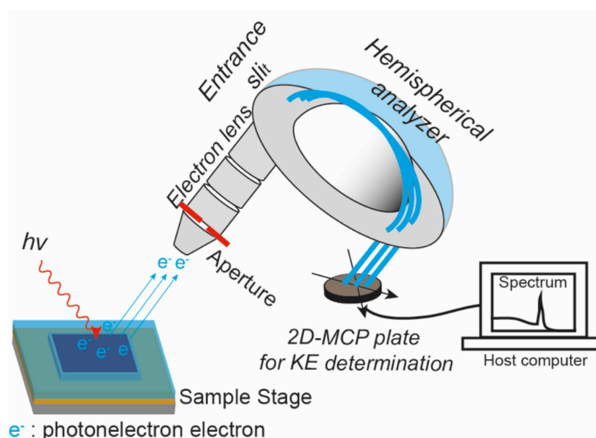

Scheme 2.5. *The basic components of an XPS instrument.*

The components of an XPS instrument are shown in Scheme 2.5. An XPS instrument essentially is composed of an X-ray source, electron extraction optics and energy filter (bandpass filter), and a detection system. The X-ray source used should have sufficient photon energy to access a proper number of core level electrons. The commonly used X-ray sources are Al Kα and Mg Kα emission sources, and synchrotron radiation. When X-rays hit the sample, photoelectrons are ejected with a series of energies and directions. The electron optics consisting of a set of electrostatic and/or magnetic lens units can collect a portion of these emitted electrons, and those electrons are transferred through the apertures. Electrostatic fields are set within the hemispherical analyzer to only allow electrons of a certain energy (pass energy) to reach the detector slits and onto the microchannel plate which is for E_{kin} determination. In order to increase the energy resolution, it is common that electrons are already decelerated with a band pass filter before they are directed to the hemispherical analyzer. The signals are transferred as spectra on

the host computer.[11] In this thesis, to characterize chemical changes in the photoresists upon EUV/DUV exposure we used two XPS instruments with a monochromatic Al Kα X-ray source (1.5 keV photon energy) at PSI (Surface Science Lab) and at ARCNL/AMOLF. Both instruments used a hemispherical energy analyzer: a SPECS Analyzer Phoibos 150 in the PSI Surface Science Lab, and a SCIENTA HIPP-3 at ARCNL/AMOLF.

When the X-ray beam is directed onto the sample, the X-ray photon energy can be absorbed by the core level electrons in the atoms. When the core-level electrons get enough energy from the photon, they will escape from the atoms. Most of the photo-emitted electrons can undergo inelastic collisions, recombination, recapture or trapping in different excited states within the sample, which can reduce the number of escaping photoelectrons. Only a small fraction of the electrons can escape from the sample surface with a certain kinetic energy E_{kin}, which can be measured by the electron spectrometer (detector). The binding energy E_{bind} of the emitted electrons can be determined by using the Einstein relationship, equation 2.5:

$$E_{bind} = E_{photon} - (E_{kin} + \psi) \tag{2.5}$$

In eq. 2.5 E_{bind} is the binding energy of the electron, E_{photon} is the energy of the X-ray photon, E_{kin} is the kinetic energy of the electron, which is measured by the instrument, and ψ is the combined work function of the spectrometer and the sample. The work function of the spectrometer is constant for a given spectrometer and can be quantified by a specific calibration by using a clean gold foil as a reference. The gold is used as reference because it is a conducting material and the measured values do not need to have an added charge correction to the reported values.[12] Contrarily, for non-conductive samples, photoelectron emission leads to surface charging, which can affect the sample work function. As the photoelectrons are ejected, positive charge can build up at the sample surface and shift the E_{kin} values. When the surface charge is stable and uniform, one practical way is to use the binding energy of C 1s from carbon species involved in C-C or C-H (285.0 eV) bonds or the binding energy of Au 4f from a gold coating (84.0 eV) as an internal standard to correct all the measured E_{bind}.[13]

Since each core-level electron has its unique binding energy, all the elements except hydrogen and helium can be identified by this technique through the binding energy measurement. The binding energy of the core-level electron is sensitive to the chemical environment. In this thesis, the XPS spectra were calibrated according to the Au $4f_{7/2}$ peak from a gold foil or the C 1s peak from hydrocarbon bonds as mentioned above before the different spectra were compared to each other to measure relative peak shifts. The schematic of XPS is shown in Scheme 2.6.

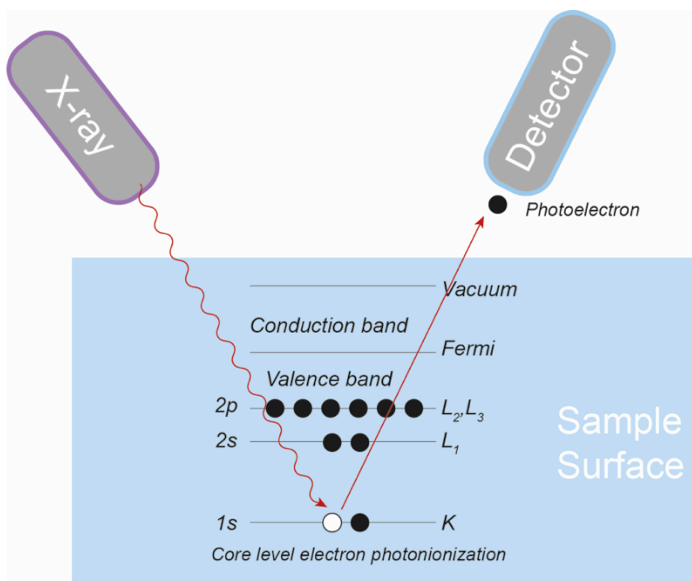

Scheme 2.6. *Mechanism of X-ray photoelectron spectroscopy.*

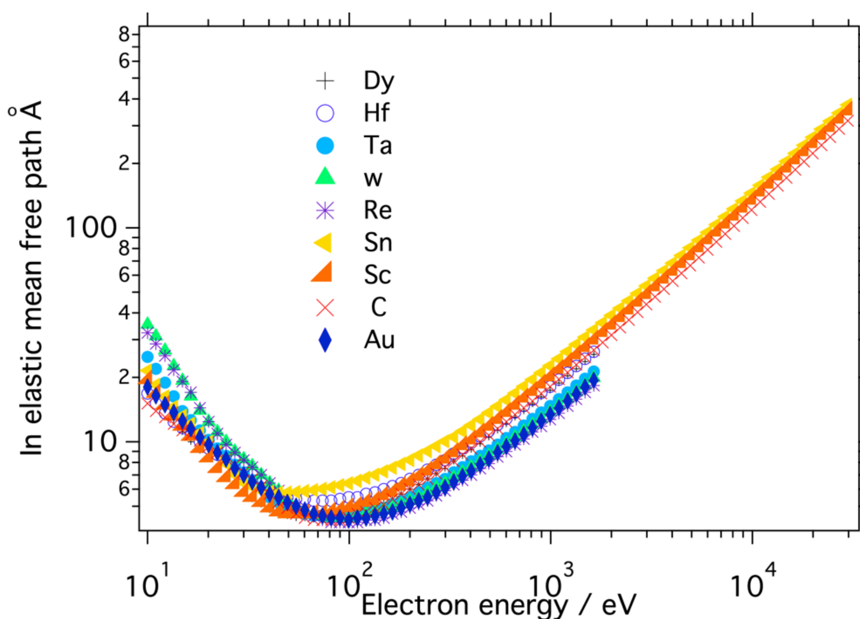

Figure 2.4. *Inelastic mean free path of electrons as a function of the electron kinetic energy in different solids.*[14-17]

The photoelectrons generated in the sample during XPS experiments with a certain kinetic energy can only travel a limited distance, which means that only the electrons emitted and escaped from near the surface of the sample can be detected. The characteristic depth d from which the emitted photoelectrons reach the detector

is called escape depth.[14, 15] When the effect from elastic electron scattering are negligible, the escape depth (ED) can be simplified as the product of the inelastic mean free path (IMFP) and cosine of electron emission angle.[17, 18] Since the emission angle is fixed for each measurement, the ED is proportional to the IMFP. The IMFP of electrons as a function of the E_{kin} in different solids is shown in Fig. 2.4.[16, 17] Based on the relationship in Fig. 2.4 and equation 2.5, with the photon energy increasing, E_{bind} is constant, and E_{kin} is increased in the same way as the photon energy. When E_{kin} increased, the mean free path of the electrons and, accordingly, the escape depth are also increased significantly.[19, 20]

When 1.5 keV X-ray condition is used, the maximum escape depth is around 5 nm from the sample surface, and thus only electrons within this depth can escape into the vacuum and be detected by the electron spectrometer. All the samples for XPS are prepared as thin films of ca. 20 nm thickness on 1×1 cm^2 substrate. To fulfill the conductivity requirement, all the substrates are pre-coated with 2 nm Cr and 18 nm Au. At PSI, the X-ray beam size is around 2×2 mm^2, which is a large area and allows to collect photoelectrons from almost the whole sample surface. At AMOLF, the X-ray beam size is around 100 μm^2. All the spectra were recorded in the transmission mode of the hemispherical analyzer. In order to compare the data with different photon energies and different equipment, the relative sensitivity factors are considered during data analysis as described below in section **2.9**.

2.8 Low dose photoelectron spectroscopy

The synchrotron based low dose photoelectron spectroscopy (Low dose PES) at the PM4 beam line (BESSY-II, Helmholtz-Zentrum-Berlin) is used for recording photoelectron spectra with excitation at relatively low photon energies.[21] It also allows us to expose the sample to EUV radiation and measure the XPS *in situ*. We made use of an angle-resolved time of flight (ArTOF) detector, which due to its high transmission (around 13%) allows for ~1000 times faster acquisition times and reduced dose rates compared to a traditional hemispherical analyzer, without losing the energy resolution.[22] In ArTOF, the full acceptance cone of the electron lens is used and a time resolved 2D detector is placed at the end of the lens where the angular pattern is projected. This design allows the simultaneous measurement of two coordinates x and y and the arrival time of the electron. When all the parameters are known with high precision, the trajectory and the corresponding velocity distribution along it, can be calculated with high precision. The kinetic energy of the emitted electrons and the emission angle also can be accurately determined.[22] By using the ArTOF, the sample change over time also can be monitored, because the spectra for each individual event are stored.[22]

Three plane gratings (150, 360 and 1228 l/mm) covering the photon energy ranges 7 – 1000, 18 – 2000 and 75 – 2000 eV are available in the PM4 beamline.[22] The photon energy range can be varied from 7 to 2000 eV by interchanging the gratings. A lower photon flux is used in this beamline for probing the samples in order to reduce radiation induced sample damage. In addition, it also reduces the sample charging problems of the non-conductive samples. Fig. 2.5 shows the photon flux as a function of photon energy for the three different gratings.

In the experiments at this beam line, due to technical difficulties we could only use the 360 l/mm grating, c_{ff} 1.7. Since the range of the photon energy is wider as from 17 to 2000 eV, both the EUV exposure (at 92 eV) and recording the full range photoelectron spectra (binding energy between 380 and 800 eV) can be realized directly at the same time without breaking the vacuum at this end station. By moving a slit out of the photon beam, the sample can be exposed to a higher dose of 92 eV photons, followed by high resolution XPS measurements at higher energies to trace the chemical changes in the samples without any contamination from the atmosphere.

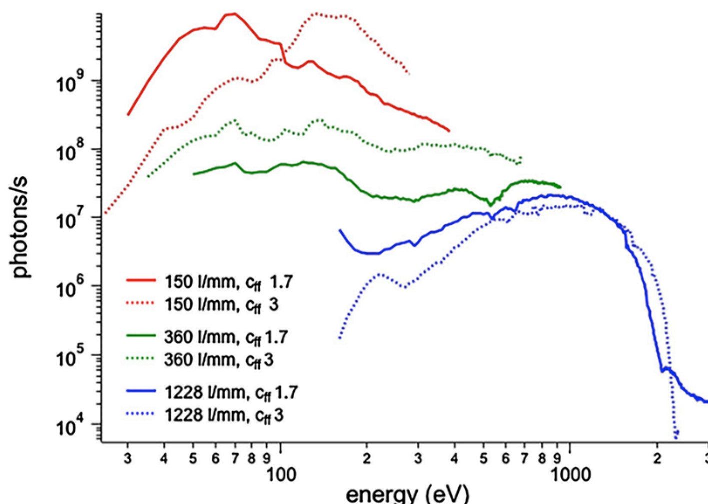

Figure 2.5. *Photon flux as a function of photon energy for the three gratings (red, green and blue colors), c_{ff} is the constant focus distance. This figure is adapted from reference 21.*

2.9 Hard X-ray photoelectron spectroscopy

The synchrotron based hard x-ray photoelectron spectroscopy (HAXPES) established at the KMC-1 beamline at the BESSY II synchrotron was also used to characterize the photoresist films. Comparing with the other XPS experiments, it provides a high photon energy from 2 to 12 keV with high photon flux of 10^{11}-10^{12}

photon s^{-1}, combined with a special electron spectrometer, the SCIENTA R-4000 hemispherical analyzer. This special electron spectrometer was designed and developed for the HAXPES and it can detect electron kinetic energies up to 15 keV and meet the high requirement of stability and resolution during the measurement. Based on Fig. 2.4, when the photon energy is around 2 - 12 keV, the probing depth could be 2 – 20 nm, it even could reach to 80 – 100 nm with porous soft materials, which means this technique with high photon energy can detect the electron from the bulk of the materials.[23] Variation of the photon energy was done to unambiguously assign spectral features to direct photoionization lines, since for the latter the electron kinetic energy increases with the incident photon energy, whereas lines arising from Auger transitions have a constant kinetic energy. The total energy resolution of the experiment, with the main contributions coming from the photon bandwidth and the electron analyzer resolution, was estimated to approx. 250 meV. The X-ray beam size is down to 100×100 μm^2 with power ~10 μW cm^{-2}, which allowed the recording of the spectrum in a few minutes without significant damage to the sample.[24] These special properties of the HAXPES open up the possibilities for the study of properties of the photoresist as thin film.[23, 25] The pressure in the experimental chamber was in the low 10^{-9} mbar range, and the samples were introduced via a load-lock chamber.

In this thesis, we mainly used 2005 eV as photon energy for HAXPES experiments. All the spectra were recorded in the transmission mode of the analyzer. The sample requirement for this measurement is the same as what has been mentioned in the XPS measurement.

For quantitative analysis of the XPS spectra, sensitivity factors (S) need to be considered, which convert the relative peak areas (I) to relative numbers of atoms (n) in the detected volume as shown in equation (2.6).[26, 27]

$$n = I/S \tag{2.6}$$

The number of photoelectrons detected per second from an orbital of constituent atoms is measured as peak area:

$$I = nf\sigma\phi yAT\beta \tag{2.7}$$

Where f is the X-ray photon flux, σ is the photoelectric cross-section, ϕ is an angular correction factor for the instrument arrangement (angle between photon path and emitted photoelectron that is detected), y is a photoelectric ground state efficiency factor, A is the area from which photoelectrons are detected, and T is the efficiency of the detection of emitted photoelectrons of that energy by the analyzer, β is the mean free path of the photoelectrons in the samples.[26, 27]

The sensitivity factor is given by:

$$S = f\sigma\phi yAT\beta \tag{2.8}$$

Seah et al. mentioned that there are three options to get the relative sensitivity factors for XPS data quantification:[27] (i) developing an own database, which is time consuming, (ii) using theoretical calculation such as the one of Seah et al.,[27] (iii) using a database such as the one based on the data from Wagner et al.[26, 28, 29] We choose the easier approach which is using the database. When the Al Kα X-ray source is used, the sensitivity factors relative to C 1s can be found from database base on Wagner et al.'s data, where they measured the data from two setups and there was a good consistency between the data from the two setups on the same compound.[26, 28, 29] When the synchrotron X-ray sources were used, regardless of the difference from the transmission function, the main difference is from the photon energy where 2005 eV is used instead of 1487 eV. We need consider the mean free path change. As shown in Fig. 2.4, the escape depths of photon electrons with different kinetic energies are different and proportional to the inelastic mean free path. At the same equipment, the electron emission angle is fixed, the larger the inelastic mean free path, the more electrons can escape to the vacuum and be detected by the analyzer. To correct the relative sensitivity factor *S'* with the escape depth β':

$$S' = \beta' S/\beta \tag{2.9}$$

Using the inelastic mean free path (from Fig. 2.4) of carbon and tin as example, the ratio between the inelastic mean free path of electron from carbon and Sn is around 1.19 when Al Kα X-ray source is used. The ratio is changed to 1.18 when the 2005 eV is used. Thus, in this case, there is no significant effect from the photon energy.

In this way, the XPS spectra at different photon energies can be analyzed quantitatively.

2.10 References

1. M. D. Tyona, "A theoritical study on spin coating technique", *Adv. Mater. Res.*, 2013, **2**, 195-208.
2. B. Cappela and G. Dietler, "Force-distance curves by atomic force microscopy", *Surf. Sci. Rep.*, 1999, **34**, 1–104.
3. N. Mojarad, J. Gobrecht and Y. Ekinci, "Interference lithography at EUV and soft X-ray wavelengths: Principles, methods, and applications", *Microelectron. Eng.*, 2015, **143**, 55-63.
4. N. Mojarad, M. Hojeij, L. Wang, J. Gobrecht and Y. Ekinci, "Single-digit-resolution nanopatterning with extreme ultraviolet light for the 2.5 nm technology node and beyond", *Nanoscale*, 2015, **7**, 4031-4037.

5. V. Auzelyte, D. Grützmacher, L. J. Heyderman, F. Luo, S. Olliges, C. Padeste, P. K. Sahoo, T. Thomson, A. Turchanin, C. David and H. H. Solak, "Extreme ultraviolet interference lithography at the Paul Scherrer Institut", *J. Micro/Nanolitho. MEMS MOEMS*, 2009, **8**, 02120401-10.
6. D. Fan and Y. Ekinci, "Photolithography reaches 6 nm half-pitch using EUV light", *Proc. SPIE*, 2016, **9776**, 97761V.
7. L. Azarnouche, E. Pargon, K. Menguelti, M. Fouchier, D. Fuard, P. Gouraud, C. Verove and O. Joubert, "Unbiased line width roughness measurements with Critical dimension Scaning Electron Microscopy and Critical Dimension Atomic Force Microscopy", *J. Appl. Phys.*, 2012, **111**, 084318.
8. T. Ohashi, T. Sekiguchi, A. Yamaguchi, J. Tanaka and H. Kawada, "Photoresist cross-sectional shape change caused by scanning electron microscope-induced shrinkage", *Proc. SPIE*, 2015, **14**, 14-18.
9. G. F. Lorusso, V. Rutigliani, F. Van Roey and C. A. Mack, "Unbiased roughness measurements: Subtracting out SEM effects", *Microelectron. Eng.*, 2018, **190**, 33-37.
10. M. Aziz and A. F. Ismail, in *Membrane Characterization*, eds. N. Hilal, A. F. Ismail, T. Matsuura and D. Oatley-Radcliffe, Elsevier, 2017, Chapter 5, 81-93.
11. P. van der Heide, in *X‐Ray Photoelectron Spectroscopy*, Wiley, 2011, Chapter 3, 27-60.
12. B. D. Ratner and D. G. Castner, in *Surface Analysis – The Principal Techniques*, eds. J. C. Vickerman and I. S. Gilmore, Wiley, 2 edn., 2009, Chapter 3, 47-112.
13. M. Jacquemin, M. J. Genet, E. M. Gaigneaux and D. P. Debecker, "Calibration of the X-Ray Photoelectron Spectroscopy Binding Energy Scale for the Characterization of Heterogeneous Catalysts: Is Everything Really under Control?", *ChemPhysChem*, 2013, **14**, 3618-3626.
14. M. P. Seah and W. A. Dench, "Quantitative electron spectroscopy of surfaces: A standard data base for electron inelastic mean free paths in solids", *Surf. Interface Anal.*, 1979, **1**, 2-11.
15. T. Akari, in *High-Resolution Spin-Resolved Photoemission Spectrometer and the Rashba Effect in Bismuth Thin Films*, Spinger, 2015, Chapter 2, 15-30.
16. Tanuma, S., C. J. Powell and D. R. Penn, "Calculations of electron inelastic mean free paths. IX. Data for 41 elemental solids over the 50 eV to 30 keV range", *Surf. Interface Anal.*, 2011, **43**, 689-713.
17. C. J. Powell and A. Jablonski, *NIST Electron Inelastic-Mean-Free-Path Database* - Version 1.2 National Institute of Standards and Technology, Gaithersburg, MD, 2010
18. A. Jablonski and C. J. Powell, "Relationships between electron inelastic mean free paths, effective attenuation lengths, and mean escape depths", *J. Electron. Spectrosc. Relat. Phenom.*, 1999, **100**, 137-160.
19. S. Tanuma, C. J. Powell and D. R. Penn, "Calculations of electron inelastic mean free paths", *Surf. Interface Anal.*, 2005, **37**, 1-14.

20. S. Tanuma, C. J. Powell and D. R. Penn, "Calculations of electron inelastic mean free paths. V. Data for 14 organic compounds over the 50–2000 eV range", *Surf. Interface Anal.*, 1994, **21**, 165-176.
21. E. Giangrisostomi, R. Ovsyannikov, F. Sorgenfrei, T. Zhang, A. Lindblad, Y. Sassa, U. B. Cappel, T. Leitner, R. Mitzner, S. Svensson, N. Mårtensson and A. Föhlisch, "Low Dose Photoelectron Spectroscopy at BESSY II: Electronic structure of matter in its native state", *J. Electron. Spectrosc. Relat. Phenom.*, 2018, **224**, 68-78.
22. R. Ovsyannikov, P. Karlsson, M. Lundqvist, C. Lupulescu, W. Eberhardt, A. Föhlisch, S. Svensson and N. Mårtensson, "Principles and operation of a new type of electron spectrometer – ArTOF", *J. Electron. Spectrosc. Relat. Phenom.*, 2013, **191**, 92-103.
23. M. Gorgoi, S. Svensson, F. Schäfers, G. Öhrwall, M. Mertin, P. Bressler, O. Karis, H. Siegbahn, A. Sandell, H. Rensmo, W. Doherty, C. Jung, W. Braun and W. Eberhardt, "The high kinetic energy photoelectron spectroscopy facility at BESSY progress and first results", *Nucl. Instrum. Methods Phys. Res., Sect. A*, 2009, **601**, 48-53.
24. Y. Zhang, J. Haitjema, X. Liu, F. Johansson, A. Lindblad, S. Castellanos, N. Ottosson and A. M. Brouwer, "Photochemical conversion of tin-oxo cage compounds studied using hard x-ray photoelectron spectroscopy", *J. Micro/Nanolitho. MEMS MOEMS*, 2017, **16**, 023510.
25. F. Schaefers, M. Mertin and M. Gorgoi, "KMC-1: a high resolution and high flux soft x-ray beamline at BESSY", *Rev. Sci. Instrum.*, 2007, **78**, 123102.
26. C. D. Wagner, L. E. Davis, M. V. Zeller, J. A. Taylor, R. H. Raymond and L. H. Gale, "Empirical atomic sensitivity factors for quantitative analysis by electron spectroscopy for chemical analysis", *Surf. Interface Anal.*, 1981, **3**, 211-225.
27. M. P. Seah, I. S. Gilmore and S. J. Spencer, "Quantitative XPS: I. Analysis of X-ray photoelectron intensities from elemental data in a digital photoelectron database", *J. Electron. Spectrosc. Relat. Phenom.*, 2001, **120**, 93-111.
28. C. D. Wagner, "Sensitivity factors for XPS analysis of surface atoms", *J. Electron. Spectrosc. Relat. Phenom.*, 1983, **32**, 99-102.
29. J. F. Moulder and J. Chastain, Handbook of X-ray Photoelectron Spectroscopy: A Reference Book of Standard Spectra for Identification and Interpretation of XPS Data, Physical Electronics Division, Perkin-Elmer Corporation, 1992.